


Influence of Fermi level position on vacancy-assisted diffusion of aluminum in zinc oxide

T. N. Sky,* K. M. Johansen, V. Venkatachalapathy, B. G. Svensson, and L. Vines
*Department of Physics and Center for Materials Science and Nanotechnology, University of Oslo,
 P.O. Box 1048 Blindern, N-0316 Oslo, Norway*

F. Tuomisto
Department of Applied Physics, Aalto University, P.O. Box 15100, FI-00076 Aalto, Espoo, Finland

 (Received 23 March 2018; revised manuscript received 4 December 2018; published 28 December 2018)

The influence of Fermi level position and annealing ambient on the zinc vacancy V_{Zn} generation and Al diffusion is studied in monocrystalline zinc oxide (ZnO). From secondary-ion mass spectrometry and positron annihilation spectroscopy results, a quadratic dependence between the concentrations of V_{Zn} and Al is established, demonstrating the Fermi level dependence of the formation of the electrically compensating -2 charge state of V_{Zn} in conductive n -type ZnO crystals. In contrast, thermal treatment in the zinc-rich ambient is shown to efficiently reduce the V_{Zn} concentration and related complexes. Using a reaction-diffusion model, the diffusion characteristics of Al at different donor background concentrations are fully accounted for by mobile $(\text{Al}_{\text{Zn}}V_{\text{Zn}})^-$ pairs. These pairs form via the migration and reaction of isolated V_{Zn}^{2-} with the essentially immobile Al_{Zn}^+ . We obtain a migration barrier for the $(\text{Al}_{\text{Zn}}V_{\text{Zn}})^-$ pair of 2.4 ± 0.2 eV, in good agreement with theoretical predictions. In addition to strongly alter the shape of the Al diffusion profiles, increasing the donor background concentration also results in an enhanced effective Al diffusivity, attributed to a reduction in the V_{Zn}^{2-} formation energy as the Fermi level position increases.

DOI: [10.1103/PhysRevB.98.245204](https://doi.org/10.1103/PhysRevB.98.245204)

I. INTRODUCTION

Vacancy-assisted impurity diffusion in semiconductors plays a central role in both device processing and fundamental understanding of the defect interplay. This is particularly true for semiconducting oxides like zinc oxide (ZnO) [1–8], where highly conductive n -type crystals (n -ZnO) can be realized by doping with, e.g., Al or Ga [9] and can be used in optoelectronics and photovoltaics. It is known, however, that self-compensation effects arise in highly doped ZnO [10], which pose a limit to the conductivity, although the exact mechanism remains somewhat controversial. For Al-containing ZnO, this has been attributed to the formation of zinc vacancies V_{Zn} and/or a complex between V_{Zn} and Al at the zinc site $(\text{Al}_{\text{Zn}}V_{\text{Zn}})$ [11].

Regardless of the crystal growth technique used, ZnO is notoriously known to exhibit n -type conductivity. Intrinsic defects such as oxygen vacancies V_{O} have long been speculated to be the origin of the unintentional n -type behavior [12]. However, more recent results conclude that V_{O} is a deep double donor [13,14], not contributing to the free-carrier concentration at room temperature. Also Zn_i can be ruled out as the source of the n -type conductivity due to its high formation energy in n -ZnO and low migration barrier of 0.55–0.70 eV [15,16], ensuring migration even at room temperature. The focus has therefore shifted to residual impurities that may affect the electrical properties. Common residual impurities in hydrothermally grown ZnO are hydrogen ($<5 \times 10^{17} \text{ cm}^{-3}$),

lithium ($\sim 10^{17} \text{ cm}^{-3}$), silicon ($\sim 10^{16} \text{ cm}^{-3}$), and aluminum ($3 \times 10^{15} \text{ cm}^{-3}$) [17]. H, Si, and Al may all increase the n -type conductivity acting as shallow donors [17], while Li has been shown to primarily reside on the zinc site acting as an acceptor in n -ZnO [18,19].

V_{Zn} is considered to be a deep acceptor in n -ZnO, with theoretical studies predicting the V_{Zn} to be in the double negatively charged state (V_{Zn}^{2-}) [13,14,20–22]. This double-acceptor behavior has also been indicated experimentally by comparing positron annihilation spectroscopy results with Hall effect data [10,23,24]. Furthermore, recent diffusion studies of Al [4] and Ga [25] in ZnO have demonstrated a quadratic dependence of the apparent diffusion coefficient on the concentration of Al or Ga. In Refs. [4,25], it was further suggested that V_{Zn}^{2-} is the dominant vehicle for the diffusion of Al/Ga through the formation of an intermittent substitutional dopant-vacancy complex.

Moreover, calculations based on density functional theory (DFT) predict the formation energy of V_{Zn} to be highly dependent not only on the Fermi level position but also on the chemical potential or annealing ambient [14]. Hence, this can be utilized to control dopant diffusion in oxides [14]. Indeed, the boiling point of zinc is sufficiently low to obtain a Zn-rich ambient during typical diffusion processes, and accordingly, ZnO is one of the few systems where metal-rich conditions can apply in practice. Thus, ZnO is an attractive model system to study the influence of the Fermi level position and ambient on impurity diffusion via charged vacancies.

In this work, we first use positron annihilation spectroscopy (PAS) and secondary-ion mass spectrometry (SIMS)

*t.n.sky@fys.uio.no

to directly observe a quadratic dependence between the V_{Zn} - and Al dopant concentrations in n -ZnO and hence the Fermi level dependence of the V_{Zn}^{2-} formation energy. Second, quasi-isococoncentration diffusion experiments have been performed in which the diffusion of Al occurs in monocrystalline ZnO containing a uniform background concentration of Ga. This enables control of the Fermi level position independently of the diffusing dopant under study. As a result, the diffusion of Al in ZnO is strongly evidenced to be mediated by V_{Zn}^{2-} , and it is suggested that this occurs through the formation of mobile and intermittent $(\text{Al}_{\text{Zn}}V_{\text{Zn}})^-$ pairs.

II. EXPERIMENT

A thin film of Al-doped ZnO with a thickness of $1.5 \mu\text{m}$ was deposited by sputtering onto different hydrothermally (HT) grown single-crystalline bulk ZnO (0001-oriented) wafers. A Semicore magnetron sputtering system was used to cosputter a 99.99% pure ZnO target with a 99.95% pure Al target to obtain a high-quality ZnO film containing $2 \times 10^{21} \text{cm}^{-3}$ Al, as determined by SIMS. After deposition, one wafer (Tokyo Denpa) with a resistivity of $1310 \Omega\text{cm}$ and measured residual bulk Al, Ga, H, Li, and Si concentrations of 3×10^{15} , 2×10^{15} , $< 5 \times 10^{17}$, 2×10^{17} , and $\leq 10^{16} \text{cm}^{-3}$, respectively, was cleaved by a laser cutter into samples with a typical size of $5 \times 5 \text{mm}^2$. The samples were then heat treated for a duration of 80 h at 1050°C (Al-1050) or for 3 h at 1200°C (Al-1200) in air before the deposited films were removed by chemical etching in a HCl solution followed by mechanical polishing and a HF dip. In addition, one Al-1050 sample was subsequently heat treated in a zinc ambient at 900°C (AlZn-900) for a duration of 2 h. For reference, one as-grown HT (Tokyo Denpa) bulk sample was treated for 3 h at 1200°C in air (AsG-1200), while another HT (SPC GoodWill) bulk sample was treated for 2 h at 900°C in a zinc ambient (Zn-900).

Another HT bulk wafer was obtained from the authors of Ref. [26] and grown by a modified HT method [26] to yield wafers with an as-grown uniform Ga concentration of $1 \times 10^{19} \text{cm}^{-3}$ and a resistivity of $7 \times 10^{-3} \Omega\text{cm}$. This wafer, labeled predoped, was subjected to a similar (but shorter) Al-doped ZnO film deposition as described above for the Tokyo Denpa wafer to yield a $0.8\text{-}\mu\text{m}$ -thick film. This was followed by sequential (isochronal) heat treatments for 30 min from 700°C up to 1150°C in intervals of 50°C . It should be noted that the slightly different HT growth technique used for the predoped sample results in a lower residual Li concentration ($< 1 \times 10^{15} \text{cm}^{-3}$) compared to $2 \times 10^{17} \text{cm}^{-3}$ for the Tokyo Denpa wafer. Table I outlines the detailed workflow of the different samples used.

Doppler broadening PAS was used to estimate the concentration and depth distribution of V_{Zn} and V_{Zn} -related complexes, where monoenergetic positrons (energy varied between 0.5 and 36 keV) were implanted into the bulk surface (0001 oriented) at room temperature. The Doppler broadened annihilation peak was measured with a HPGGe detector (FWHM of energy resolution of 1.2 at 511 keV) and analyzed by the conventional S and W parameters. Here, S is defined as the fraction of the counts in the central region (corresponding to electron-positron momentum of < 0.4 a.u.) of the

TABLE I. Detailed overview of the experimental sample sequential treatments.

Sample	Film	Anneal	Polished	Anneal
Al-1050	Al:ZnO	80 h, 1050°C	yes	
Al-1200	Al:ZnO	3 h, 1200°C	yes	
AlZn-900	Al:ZnO	80 h, 1050°C	yes	2 h, 900°C
AsG-1200		3 h, 1200°C		
Zn-900		2 h, 900°C		
Predoped	Al:ZnO	$\frac{1}{2}$ h, $700^\circ\text{C} \rightarrow 1150^\circ\text{C}$		

annihilation line to the total number of counts in the spectrum [27]. Similarly, W represents the fraction of the counts in the wing region (corresponding to electron-positron momentum $> 1.6\text{--}2.0$ a.u.) [27].

To monitor the depth redistributions of Al and Ga, a Cameca IMS 7f SIMS instrument equipped with an O_2 primary ion beam source was used. Absolute concentrations were obtained by measuring separate Al- and Ga-implanted reference samples, ensuring less than $\pm 10\%$ error in accuracy. A Dektak 8 stylus profilometer was used to measure the sputtered crater depths, and a constant erosion rate as a function of time was assumed.

III. RESULTS AND DISCUSSION

A. Formation of V_{Zn}

Figure 1 shows the Al concentration vs depth profiles for the samples heat treated at 1050°C (Al-1050) and 1200°C (Al-1200) for 80 and 3 h, respectively. Also shown are the Al profiles in the reference samples AsG-1200 and Zn-900. The Al concentration is almost uniform at a level of $\sim 2 \times 10^{19}$

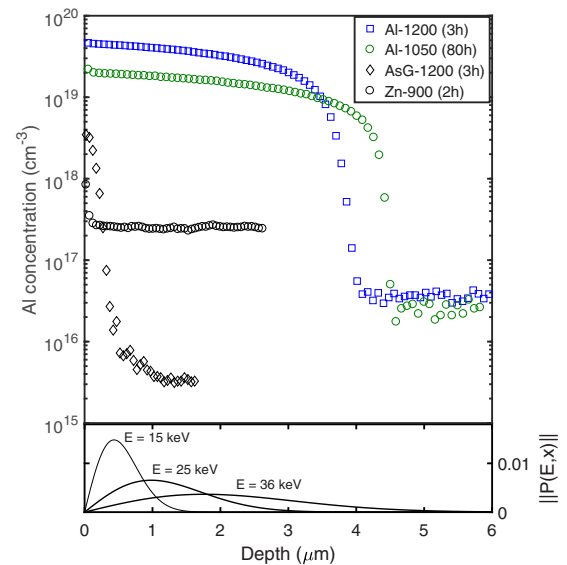


FIG. 1. Al concentration vs depth profiles of the intentionally doped samples Al-1050 and Al-1200 and of the reference samples AsG-1200 and Zn-900, as measured by SIMS. Also shown (solid lines in the bottom panel) are the calculated positron implantation profiles $P(x, E)$ for a representative range of implantation energies E .

and $\sim 4 \times 10^{19} \text{ cm}^{-3}$ in the first 4–5 μm for samples Al-1050 and Al-1200, respectively. For AsG-1200 and Zn-900, the Al concentration is several orders of magnitude lower. Note that the Zn-900 sample originates from a different supplier (SPC GoodWill) than AsG-1200 and exhibits a higher as-grown residual Al concentration ($\sim 2 \times 10^{17} \text{ cm}^{-3}$).

In the event of monoenergetic positrons impinging onto a solid surface, the resulting implanted positron distribution can be expressed by a Makhov profile [28–30]. A representative selection of the Makhov profiles is included in the bottom panel of Fig. 1 (solid lines), illustrating the probing depth of the implanted positrons in a Doppler broadening measurement. The results of the Doppler broadening PAS measurements, as given by the S parameter vs positron implantation energy, are shown in Fig. 2 for the different samples presented in Fig. 1, together with that for the AlZn-900 sample. In addition, the results for a vapor phase bulk ZnO sample (ZnO lattice) are included, referencing the V_{Zn} -lean extremity (cf. [23]). The signal originating from the first $\sim 300 \text{ nm}$ below the surface is affected by surface annihilations and, in particular, recombination with defects induced from mechanical polishing [31]. For that reason, only data points corresponding to $15 \leq E \leq 36 \text{ keV}$ will be discussed below. The inset in Fig. 2 shows the corresponding S - W plot, where all the data follow the same line connecting the vacancy-lean (ZnO lattice) and V_{Zn} -saturated cases. This indicates that V_{Zn} or complexes with a similar open volume are the dominating defect in samples Al-1050, Al-1200, and AsG-1200. A high S -parameter value is found for the intentionally Al doped samples, indicating an increased concentration of V_{Zn} and/or V_{Zn} -related complexes. Interestingly, V_{Zn} disappears below the detection limit ($< 10^{15} \text{ cm}^{-3}$) in the Al-doped sample after subsequent treatments in Zn-rich ambient at 900°C for 2 h (AlZn-900). This demonstrates introduction of Zn interstitials

and recombination with V_{Zn} during the Zn-rich treatment and hence an increased formation energy of V_{Zn} under Zn-rich conditions, as proposed by DFT results [14]. Thus, thermal treatments in a Zn-rich ambient appear to be a viable route for reducing the concentration of V_{Zn} and related complexes. Here, it should be underlined that the presence of Al_{Zn} as 1 of the 12 next-nearest neighbors to V_{Zn} [11] is not resolved by the PAS measurement [32]. Hence, it is not possible to discern an isolated V_{Zn} from a $\text{Al}_{\text{Zn}}V_{\text{Zn}}$ pair using the PAS results.

Sample Al-1200, which exhibits the highest Al concentration (Fig. 1), also reveals the highest relative concentration of V_{Zn} (Fig. 2). This is in agreement with first-principles calculations [13,14,20–22] predicting a decrease in the V_{Zn}^{2-} and V_{Zn}^- formation energy as the Fermi level position increases. From the PAS results (Fig. 2), the V_{Zn} concentration can be estimated using [27]

$$C_{V_{\text{Zn}}} = \frac{\rho}{\mu} \lambda_B \frac{S - S_L}{S_V - S}, \quad (1)$$

where $\rho = 8.3 \times 10^{22} \text{ cm}^{-3}$ is the atomic density of ZnO, $\mu = 3 \times 10^{15} \text{ s}^{-1}$ is the positron trapping coefficient for negatively charged vacancies at room temperature, and $\lambda_B = 6 \times 10^9 \text{ s}^{-1}$ is the annihilation rate in the ZnO lattice. S is the measured S parameter, and $S_L = 1$ and $S_V = 1.050$ are used as the normalized parameters for the ZnO lattice annihilation and the V_{Zn} annihilation, respectively [23,24,32,33]. Figure 3 shows the estimated V_{Zn} concentration from Eq. (1) vs the corresponding weighted mean of the Al concentration for samples Al-1050 and Al-1200 at different positron implantation energies. The weighted mean concentration is determined by weighting the measured Al profiles by the Makhov profiles (see Fig. 1). As evident from Fig. 3, there is a strong relation between the concentrations of V_{Zn} and Al. Assuming that the charge carrier concentration is in an extrinsic regime, that is, governed by the Al concentration, the slope of the line b

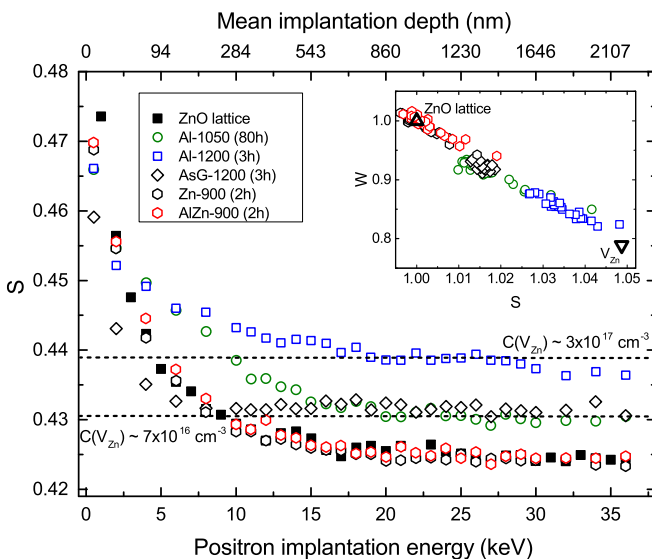


FIG. 2. S parameter vs positron implantation energy for the intentionally doped samples Al-1050, Al-1200, and AlZn-900 and for the undoped reference samples AsG-1200 and Zn-900. The dashed lines show the corresponding concentrations of V_{Zn} , as estimated by Eq. (1). The inset displays the normalized S and W parameters.

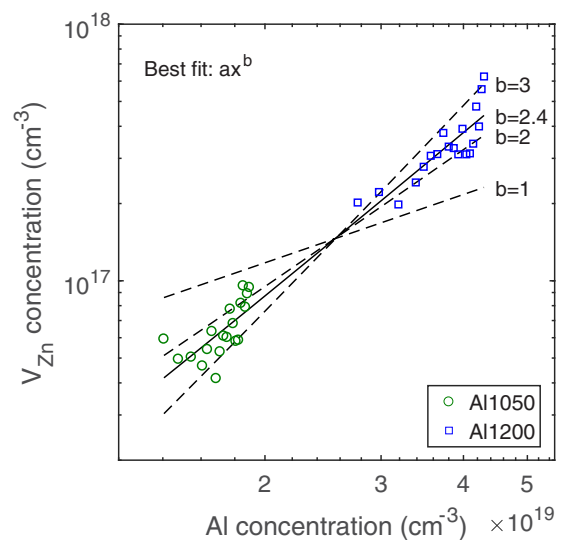


FIG. 3. V_{Zn} concentration vs Al concentration, as measured by PAS and SIMS, respectively. The straight solid line shows the best least-squares fit to the combined data with a slope of $b = 2.4$. Also shown (dotted lines) are the best fits with the constraints $b = 1, 2$, and 3 .

in Fig. 3 should be given by the charge state of V_{Zn} at the given condition. The best least-squares power series fit (ax^b) to the experimental data exhibits a slope of $b = 2.4 \pm 0.2$. Also shown in Fig. 3 are the best fits with the constraints $b = 1, 2$, and 3 . Here, it should be underlined that also the heat treatment temperature plays a role in the resulting $C_{V_{Zn}}$, and at a given Al concentration a higher $C_{V_{Zn}}$ can be expected for the Al-1200 sample than for the Al-1050 one. This is corroborated by the significant value of $C_{V_{Zn}}$ observed for the (undoped) AsG-1200 control sample (Fig. 2). Hence, the slope of $b = 2.4$ contains also a “thermal contribution” which may account for the slight deviation from a quadratic dependence in Fig. 3. Accordingly, the data in Fig. 3 strongly suggest that -2 is the prevailing charge state of V_{Zn} in the intentionally doped samples.

B. Dopant diffusion vs Fermi level position

The relation between V_{Zn}^{2-} and the Al concentration (Fig. 3) encourages investigation of the Al diffusion at different Fermi level positions, i.e., tuning the availability of V_{Zn}^{2-} in the bulk ZnO. Similar to that observed for Al, Ga doping has been shown to yield highly conductive ZnO samples [34–36]. In addition, the diffusion of Ga in ZnO has been demonstrated to exhibit characteristic boxlike depth profiles similar to those observed for Al [4,25,37], although holding a slightly higher diffusivity.

Figure 4 shows the Al and Ga concentration vs depth distributions for the predoped sample (see Table I) after sequential heat treatments (30 min) from 700 °C to 1150 °C. At 850 °C, in-diffusion of Al becomes detectable. The characteristics of the Al diffusion profiles in Fig. 4 deviate strongly from those in Fig. 1 and those previously reported in Ref. [4], where steeper slopes at the diffusion fronts were observed. It can be noted that the about two orders of magnitude higher concentration of Al in the deposited film, compared to that in the bulk, merely indicates that the ambient conditions

(vacuum/argon) during deposition cause supersaturation of Al in the heavily Al doped film. Furthermore, Ga migrates from the bulk to the film/bulk interface already at 700 °C and into the Al-doped film with an apparent solid solubility of $3\text{--}4 \times 10^{19} \text{ cm}^{-3}$ for $T_c \geq 800 \text{ °C}$. Moreover, at 800 °C–900 °C the Ga diffusion profiles resemble that of a complementary error function [$\text{erfc}(-x)$, with x being the distance from the interface], i.e., an analytical solution of Fick’s law for diffusion in a semi-infinite solid with a constant diffusion source.

As the temperature is increased above 1000 °C, the shape of the Al profiles in Fig. 4 exhibit an increased flattening in the shoulder region. This occurs when the bulk surface concentration (apparent solid solubility) of Al exceeds the predoped level of Ga in the bulk ($1 \times 10^{19} \text{ cm}^{-3}$). Below this level, which will be referred to as the “isoconcentration regime,” the Al bulk surface concentration at all the different temperatures (850 °C–1000 °C) approximately equals the predoped level of Ga. Interestingly, in this regime the in-diffusion of Al is associated with an equal out-diffusion of Ga, such that the total content of dopants (Al+Ga) within the in-diffused region is maintained. This represents an isoconcentration regime that for true tracer diffusion conditions results in diffusion without an electrochemical potential gradient present, thus yielding erfc-like profiles [38]. However, in our case, with similar but not identical dopants, such an approach slightly overestimates the experimental profiles (not shown). The slightly more mobile Ga dopants [25] diffuse out of the bulk (to the film), and a net loss of total dopants occurs in the bulk (deep end of the Al profiles) after Al in-diffusion (compare the Ga concentration at depths beyond the Al tail before and after diffusion). This gives a contribution to the electrochemical potential gradient and a small (retarded) deviation from an erfc behavior. Not surprisingly, this non-erfc behavior becomes even more pronounced above the isoconcentration regime ($T_c > 1000 \text{ °C}$), where the apparent Al solubility is well above the background concentration of Ga, resulting in a larger gradient in the electrochemical potential.

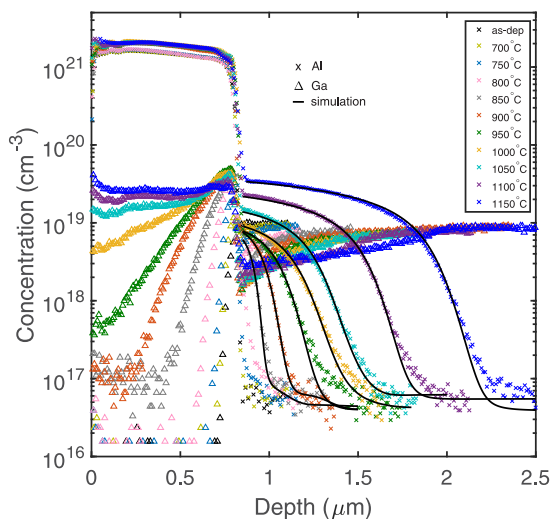
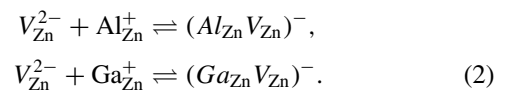


FIG. 4. Experimental Al (crosses) and Ga (triangles) concentrations vs depth distribution of the predoped sample sequentially heat treated for 30 min from 700 °C to 1150 °C. The solid lines show the best fit to the experimental Al diffusion profiles (from 850 °C).

1. Reaction diffusion model

From the above discussion, both Al and Ga need to be considered in order to account for the experimental Al diffusion data in Fig. 4. As previously shown for both Al and Ga in undoped ZnO [4,25,39], their diffusion can be explained via a mechanism invoking Al-/Ga-vacancy pairs. The pairs form and break up according to the following reactions:



In our reaction diffusion (RD) modeling, the deposited film of highly Al doped ZnO at the bulk crystal surface is considered as a source of $(Al_{Zn}V_{Zn})^-$ pairs. That is, already formed $(Al_{Zn}V_{Zn})^-$ pairs are injected into the bulk, and their flux is treated as a boundary condition in the simulations. As discussed in our previous report on Ga diffusion in ZnO [25], this assumption is corroborated by several theoretical and experimental results in the literature for both Al- and Ga-doped ZnO [4,10,11,21,40]. DFT calculations predict a low formation energy of $(Al_{Zn}V_{Zn})^-$ and $(Ga_{Zn}V_{Zn})^-$ pairs in highly n type samples under conditions comparable to

those in the present experiments [4,21,40]. This prediction is supported by electron paramagnetic resonance spectroscopy measurements [11], revealing that $(\text{Al}_{\text{Zn}}\text{V}_{\text{Zn}})^{-}$ prevails over V_{Zn} and Al_{Zn} in electron-irradiated Al-containing (10^{17} cm^{-3}) ZnO. Moreover, in a study using synchrotron x-ray absorption measurements combined with DFT [40] it was evidenced that the $(\text{Al}_{\text{Zn}}\text{V}_{\text{Zn}})^{-}$ pair is responsible for the suppressed net carrier concentration in highly Al doped ZnO samples. Based on these arguments, a high steady-state concentration of $(\text{Al}_{\text{Zn}}\text{V}_{\text{Zn}})^{-}$ pairs is expected to prevail in the Al-doped film. We can write the following full system of reaction-diffusion equations, with time t and position x :

$$\begin{aligned} \frac{\partial C_{(\text{Al}_{\text{Zn}}\text{V}_{\text{Zn}})^{-}}}{\partial t} &= D_{(\text{Al}_{\text{Zn}}\text{V}_{\text{Zn}})^{-}} \frac{\partial^2 C_{(\text{Al}_{\text{Zn}}\text{V}_{\text{Zn}})^{-}}}{\partial x^2} - \frac{\partial C_{\text{Al}_{\text{Zn}}^{+}}}{\partial t}, \\ \frac{\partial C_{(\text{Ga}_{\text{Zn}}\text{V}_{\text{Zn}})^{-}}}{\partial t} &= D_{(\text{Ga}_{\text{Zn}}\text{V}_{\text{Zn}})^{-}} \frac{\partial^2 C_{(\text{Ga}_{\text{Zn}}\text{V}_{\text{Zn}})^{-}}}{\partial x^2} - \frac{\partial C_{\text{Ga}_{\text{Zn}}^{+}}}{\partial t}, \end{aligned} \quad (3)$$

with

$$\begin{aligned} \frac{\partial C_{\text{Al}_{\text{Zn}}^{+}}}{\partial t} &= \nu C_{(\text{Al}_{\text{Zn}}\text{V}_{\text{Zn}})^{-}} - 4\pi R_c D_{\text{V}_{\text{Zn}}^{2-}} C_{\text{Al}_{\text{Zn}}^{+}} C_{\text{V}_{\text{Zn}}^{2-}}, \\ \frac{\partial C_{\text{Ga}_{\text{Zn}}^{+}}}{\partial t} &= \nu C_{(\text{Ga}_{\text{Zn}}\text{V}_{\text{Zn}})^{-}} - 4\pi R_c D_{\text{V}_{\text{Zn}}^{2-}} C_{\text{Ga}_{\text{Zn}}^{+}} C_{\text{V}_{\text{Zn}}^{2-}}. \end{aligned} \quad (4)$$

Here, $R_c = 1 \text{ nm}$ is the effective radius for capturing $\text{V}_{\text{Zn}}^{2-}$ by Al_{Zn} or Ga_{Zn} , while $\nu = \nu_0 e^{-[E_b + E_m(\text{V}_{\text{Zn}}^{2-})]/k_B T}$ is the dissociation rate of the dopant-vacancy pair, with E_b being the binding energy of the dopant-vacancy pair, $E_m(\text{V}_{\text{Zn}}^{2-})$ being the migration barrier of $\text{V}_{\text{Zn}}^{2-}$, k_B being the Boltzmann constant, and T being the temperature in degrees Kelvin. In the simulations, we assume an attempt frequency $\nu_0 = 10^{13} \text{ s}^{-1}$ for the dissociation, i.e., the characteristic oscillation frequency of the lattice, and use $E_b(\text{Al}_{\text{Zn}}\text{V}_{\text{Zn}})^{-} = 1.31 \text{ eV}$ and $E_b(\text{Ga}_{\text{Zn}}\text{V}_{\text{Zn}})^{-} = 1.25 \text{ eV}$, as previously predicted from theory [39].

At the interface between the highly n type deposited film and the bulk crystal surface, the abrupt change in the Al dopant distribution gives rise to an electric field and thus energy band bending. The effect of a spatially varying Fermi level upon dopant diffusion has previously been shown to cause an additional drift component for all defects involved in the diffusion process, resulting in an enhancement in the dopant diffusion by a factor between 1 (intrinsic) and 2 (far extrinsic) [41]. However, in a previous report of dopant diffusion [42], this effect was shown to have negligible importance for dopant diffusion at extrinsic conditions, and any drift component to the diffusion has therefore been omitted in the present work.

As indicated in Refs. [4,25], the transport capacity/coefficient of $\text{V}_{\text{Zn}}^{2-}$ is much higher than that of the dopant-vacancy pair ($C_{\text{V}_{\text{Zn}}^{2-}} D_{\text{V}_{\text{Zn}}^{2-}} \gg C_{(X_{\text{Zn}}\text{V}_{\text{Zn}})^{-}} D_{(X_{\text{Zn}}\text{V}_{\text{Zn}})^{-}}$ for $X \in \{\text{Al}, \text{Ga}\}$) and is the reason for the abrupt diffusion fronts observed for Al/Ga in undoped ZnO (see Fig. 1 and Refs. [4,25]). This means that, at steady-state conditions, the distribution of $\text{V}_{\text{Zn}}^{2-}$ will effectively be controlled only by the charge neutrality of the system,

$$n = C_{\text{Al}_{\text{Zn}}^{+}} + C_{\text{Ga}_{\text{Zn}}^{+}} - C_{(\text{Al}_{\text{Zn}}\text{V}_{\text{Zn}})^{-}} - C_{(\text{Ga}_{\text{Zn}}\text{V}_{\text{Zn}})^{-}} - 2C_{\text{V}_{\text{Zn}}^{2-}}. \quad (5)$$

Further, as outlined in Ref. [4], the concentration of $\text{V}_{\text{Zn}}^{2-}$ hinges on both the local Fermi level position and temperature:

$$C_{\text{V}_{\text{Zn}}^{2-}}(\epsilon_F, T) = \frac{\rho}{2} e^{-\frac{E_{f,0}(\text{V}_{\text{Zn}}^{2-}) - 2\epsilon_F}{k_B T}}, \quad (6)$$

where $\rho/2$ is the number of lattice sites in the zinc sublattice and $E_{f,0}(\text{V}_{\text{Zn}}^{2-})$ is the formation energy of $\text{V}_{\text{Zn}}^{2-}$ where the local Fermi level ϵ_F is positioned at the valence band maximum. ϵ_F can be approximated as

$$\epsilon_F(n, T) = E_c(T) + k_B T \ln\left(\frac{n}{N_c(T)}\right), \quad (7)$$

where $E_c(T)$ is the position of the conduction band edge relative to the valence band edge (i.e., the band gap $E_g = E_c$) and $N_c(T)$ is the conduction band effective density of states. The narrowing of the band gap, from 3.3 eV at room temperature, as a function of increasing temperature is taken as $\Delta E_g = 80.5 - 0.52T$ (meV), as extrapolated from band-gap measurements in the temperature range $100 \text{ }^{\circ}\text{C} - 500 \text{ }^{\circ}\text{C}$ by Hauschild *et al.* [43]. Combining Eqs. (6) and (7) gives the concentration of $\text{V}_{\text{Zn}}^{2-}$ as a function of the charge carrier concentration and temperature:

$$C_{\text{V}_{\text{Zn}}^{2-}}(n, T) = \frac{\rho}{2} e^{-\frac{E_{f,0}(\text{V}_{\text{Zn}}^{2-}) - 2E_c(T)}{k_B T}} \left(\frac{n}{N_c(T)}\right)^2. \quad (8)$$

This implies that the diffusion of Al and Ga is described by solving the semilinear diffusion equations of the dopant-vacancy pairs [Eq. (3)], with their association and dissociation rates described by Eq. (4) and with the concentration of $\text{V}_{\text{Zn}}^{2-}$ given by Eq. (8). Note that, solving Eq. (8) requires a value of the formation energy of $\text{V}_{\text{Zn}}^{2-}$ when ϵ_F is at the valence band maximum ($E_{f,0}(\text{V}_{\text{Zn}}^{2-})$). For this, we are guided by estimates from previous DFT reports [14,21,22,39] and set $E_{f,0}(\text{V}_{\text{Zn}}^{2-}) = 7.4 \text{ eV}$. Hence, using Eq. (8), depth profiles of $C_{\text{V}_{\text{Zn}}^{2-}}$ can be estimated numerically if $n(x)$ is known. We note further that, as long as the transport capacity of $\text{V}_{\text{Zn}}^{2-}$ is higher than that of the dopant-vacancy pair, $E_m(\text{V}_{\text{Zn}}^{2-})$ is not needed to solve the full system of differential equations [Eqs. (3), (4), (5), and (8)]. This was shown in Ref. [25] for Ga diffusion, where $E_m(\text{V}_{\text{Zn}}^{2-})$, which is inherent in both ν and $D_{\text{V}_{\text{Zn}}^{2-}}$, cancels at these conditions of the transport capacities.

2. Al diffusion energetics

The results of the reaction-diffusion simulations giving the best fit to the experimental Al profiles are shown as solid lines in Fig. 4. The corresponding extracted diffusivities vs the inverse absolute temperature are given in Fig. 5, and similarly, the extracted solubilities are depicted in Fig. 6. Both the diffusion parameters for the Al-vacancy pair and the effective Al diffusion are presented, where the former are extracted directly from the reaction-diffusion equations. For the latter, the apparent Al solid solubility, denoted by C_{Al}^S , is taken as the measured concentration of Al at the bulk surface $C_{\text{Al}}(x_{\text{bulk}} = 0)$, and the effective Al diffusivity is deduced as follows; provided that the Al atoms mainly dissolve substitutionally at the zinc site (with $C_{\text{Al}_{\text{Zn}}} \gg C_{\text{Al}_{\text{Zn}}\text{V}_{\text{Zn}}}$) and that $(\text{Al}_{\text{Zn}}\text{V}_{\text{Zn}})^{-}$ is the predominant Al diffusing species, the effective diffusivity

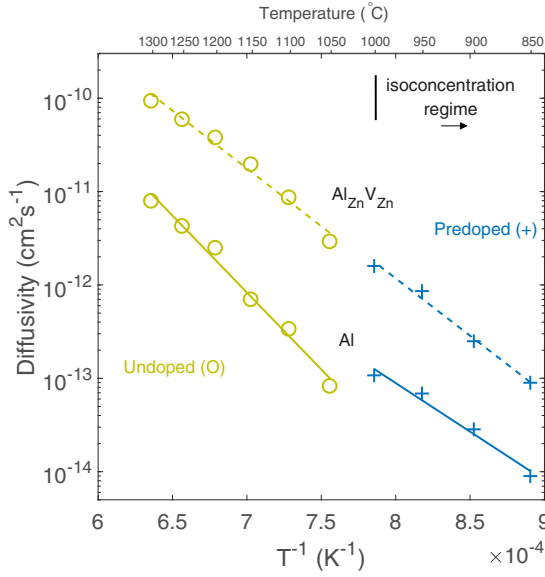


FIG. 5. Apparent diffusivities vs inverse absolute temperature of the $\text{Al}_{\text{Zn}}\text{V}_{\text{Zn}}$ pair in undoped ZnO (from Ref. [4], circles) and in predoped ZnO (crosses). Also shown are the effective diffusivity values D_{Al} (solid lines), as estimated from Eq. (9). For the predoped sample, only diffusivities in the isoconcentration regime (i.e., below 1050°C) are included.

of Al under local equilibrium conditions can be expressed by (cf. [41,44,45])

$$D_{\text{Al}} = \frac{C_{\text{Al}_{\text{Zn}}\text{V}_{\text{Zn}}}^S D_{\text{Al}_{\text{Zn}}\text{V}_{\text{Zn}}}}{C_{\text{Al}_{\text{Zn}}}^S}. \quad (9)$$

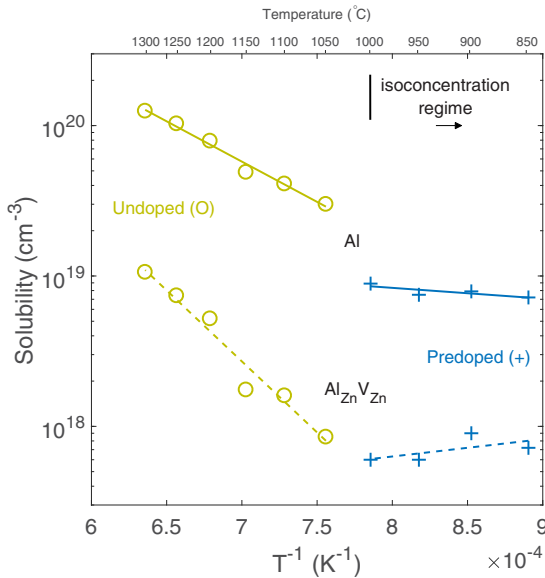


FIG. 6. Apparent solubilities vs inverse absolute temperature of the $\text{Al}_{\text{Zn}}\text{V}_{\text{Zn}}$ pair in undoped ZnO (from Ref. [4], circles) and in predoped ZnO (crosses). Also shown are the apparent Al solid solubility values $C_{\text{Al}}^S = C_{\text{Al}}(x_{\text{bulk}} = 0)$ (solid lines), as measured by SIMS. For the predoped sample, only solubilities in the isoconcentration regime (i.e., below 1050°C) are shown.

TABLE II. Diffusivity and solubility values for $\text{Al}_{\text{Zn}}\text{V}_{\text{Zn}}$ and Al in undoped ZnO [4] and predoped ZnO (isoconcentration regime), as found from the least-squares best fit of the extracted values in Figs. 5 and 6.

Process	Undoped		Predoped	
	E_m, E_a, E_f (eV)	D_0, C_0^S ($\text{cm}^2 \text{s}^{-1}, \text{cm}^{-3}$)	E_m, E_a, E_f (eV)	D_0, C_0^S ($\text{cm}^2 \text{s}^{-1}, \text{cm}^{-3}$)
$D_{\text{Al}_{\text{Zn}}\text{V}_{\text{Zn}}}$	2.5 ± 0.2	8×10^{-3}	2.4 ± 0.2	8×10^{-3}
D_{Al}	3.3 ± 0.2	3×10^{-1}	2.0 ± 0.3	2×10^{-5}
$C_{\text{Al}_{\text{Zn}}\text{V}_{\text{Zn}}}^S$	1.9 ± 0.2	1×10^{25}	-0.2 ± 0.3	7×10^{16}
C_{Al}^S	1.1 ± 0.1	3×10^{23}	0.1 ± 0.1	3×10^{19}

Here, $C_{\text{Al}_{\text{Zn}}}^S$ is taken as the apparent solid solubility C_{Al}^S as measured by SIMS, and $C_{\text{Al}_{\text{Zn}}\text{V}_{\text{Zn}}}^S$ is extracted from the simulations at $x_{\text{bulk}} = 0$. For comparison, previous experimental data of Al diffusion in undoped ZnO [4] have been remodeled using the simulation parameters as described above, and the corresponding values are included in Figs. 5 and 6 (circles). As seen in Fig. 6, the predoped sample reveals apparent solubilities with almost no temperature dependence in the interval 850°C – 1000°C (isoconcentration regime). As implied above, this weak temperature dependence arises because the sample is predoped to concentrations above the equilibrium solid solubility limit of Al at 1000°C and below. Table II lists all the extracted activation energies and preexponential factors deduced from Figs. 5 and 6.

The migration activation energy for the Al-vacancy pair in the isoconcentration regime is found to be $E_m(\text{Al}_{\text{Zn}}\text{V}_{\text{Zn}})^- = 2.4$ eV (see Fig. 5 and Table II). Within the uncertainties given in Table II, this is identical to that found in undoped ZnO (2.5 eV). Indeed, since the migration activation energy of the pair represents only the barrier required for Al to jump to an already associated V_{Zn} , no influence by the Fermi level position is anticipated. This result supports the validity of our simulation and model and the DFT values used as input. Further, the overall activation energy E_a for the diffusion of Al in the predoped sample (isoconcentration regime) is found to be, within the uncertainties given in Table II, similar to the migration barrier of the pair. This is a consequence of the similar temperature dependences of $C_{\text{Al}_{\text{Zn}}\text{V}_{\text{Zn}}}^S$ and C_{Al}^S [see Eq. (9)]. In contrast, for the undoped sample $E_a(\text{Al})$ is 0.8 eV higher than $E_m(\text{Al}_{\text{Zn}}\text{V}_{\text{Zn}})^-$, reflecting the higher $E_f(\text{V}_{\text{Zn}}^{2-})$ in this more resistive sample. Also notice that D_{Al} is higher in the predoped ZnO, which is a result of the reduced $E_f(\text{V}_{\text{Zn}}^{2-})$.

In the simulations for the undoped sample, we have used a prefactor for $D_{\text{V}_{\text{Zn}}^{2-}}$ of $D_0(\text{V}_{\text{Zn}}^{2-}) = 10^{-2}$ cm^2/s , which reflects the crystal geometry of ZnO and assumes no migration or formation entropy contribution. However, it was recently demonstrated by Azarov *et al.* [46] that Ga doping ZnO strongly enhances the Zn self-diffusion in ZnO and, in particular, that $D_0(\text{V}_{\text{Zn}}^{2-})$ scales with the Ga concentration. Accordingly, we have used a slightly higher value (by a factor of ~ 10) for $D_0(\text{V}_{\text{Zn}}^{2-})$ in the simulations for the predoped sample (1.2×10^{-1} cm^2/s). As a result, the two $D_{\text{Al}_{\text{Zn}}\text{V}_{\text{Zn}}}$ lines in Fig. 5 align (as anticipated) and support an entropy contribution of $2.5k_B$ for the diffusion of $\text{V}_{\text{Zn}}^{2-}$ in the predoped sample.

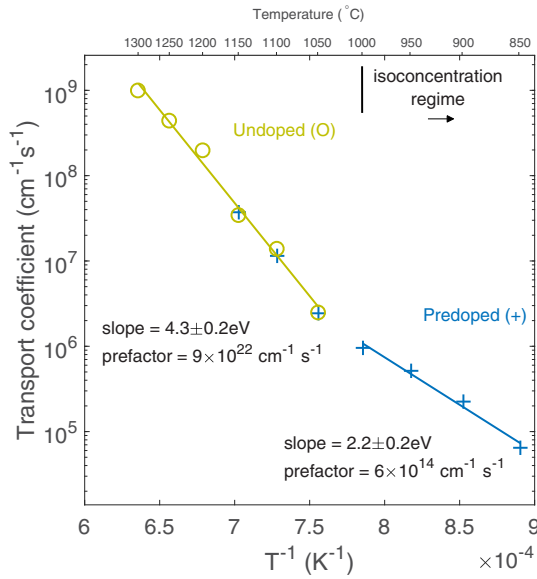


FIG. 7. Comparison of the transport coefficients vs inverse absolute temperature for Al in undoped ZnO (Ref. [4], circles) and in predoped ZnO (crosses).

Figure 7 shows the Arrhenius behavior of the Al transport coefficients/capacity ($C_{\text{Al}_{\text{Zn}}V_{\text{Zn}}}^S D_{\text{Al}_{\text{Zn}}V_{\text{Zn}}}$ or $C_{\text{Al}_{\text{Zn}}}^S D_{\text{Al}}$) for the undoped and predoped samples. Within the isoconcentration regime, the transport coefficients reveal a pronounced increase compared to the expected and extrapolated data for the undoped sample at similar temperatures. This can be explained by the fact that the exponential decrease in $C_{\text{Al}_{\text{Zn}}}^S$ with ϵ_F [$E_f(\text{Al}_{\text{Zn}}^+)$ is proportional to ϵ_F] is overruled by the squared exponential increase in D_{Al} with ϵ_F [$E_f(V_{\text{Zn}}^{2-})$ has a -2 dependence on ϵ_F]. Hence, their product increases as ϵ_F moves towards the conduction band minimum. On the other hand, above the isoconcentration regime the transport capacity of Al in the predoped sample is comparable to that in the undoped sample (Fig. 7). This is somewhat unexpected when considering the different diffusion characteristics of Al in the undoped and predoped samples illustrated in Fig. 8, where we compare the profiles after the 1100 °C anneal. One reason for this similarity in transport coefficient may be that the in-diffusion of Al is not controlled by the actual Al solid solubility but rather limited by the rate of transport of Al from the deposited film into the bulk crystal at high temperatures. This may in turn be interpreted in terms of a restriction in the formation of $(\text{Al}_{\text{Zn}}V_{\text{Zn}})^-$ pairs in the film and/or an interfacial barrier.

The demonstrated Fermi level dependence of the Al diffusion strongly suggests that the diffusion of Al is mediated by V_{Zn} . Other diffusion mechanisms may possibly result in similar profiles; however, the most likely alternative candidates can arguably be ruled out based on our experimental results. For instance, if the diffusion of interstitial Al prevailed in the bulk, either (i) as a vacancy-assisted dissociation process or (ii) through kick out by interstitial Zn, an enhanced Al diffusivity at increased ϵ_F is not expected. In both such cases, the increased ϵ_F would likely cause the effective diffusivity of

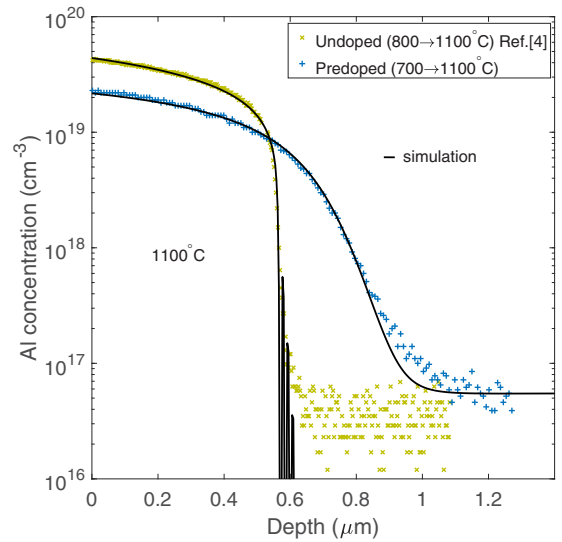


FIG. 8. Comparison of the experimental Al diffusion profiles at 1100 °C in two samples with different donor background concentrations, undoped ($\sim 3 \times 10^{13} \text{ cm}^{-3}$, Ref. [4]) and predoped ($1 \times 10^{19} \text{ cm}^{-3}$). For clarity, the deposited films have been excluded, and the film-bulk interface has been set to zero at the abscissa. The temperature intervals indicate the prehistory of the sequential 30-min heat treatments in steps of 50 °C.

Al to decrease due to (i) a high concentration of V_{Zn} traps or (ii) a low concentration of interstitial zinc available to kick out substitutional Al. Moreover, Al diffusion proceeding through a direct interstitial mechanism can also be excluded as it would yield erfc-like profiles with no dependence on ϵ_F .

IV. SUMMARY

We have studied the influence of Al doping on the formation of V_{Zn} in single-crystalline ZnO by using a combination of SIMS and PAS analysis. Conversely, we have also investigated how the supply of zinc vacancies affects the diffusion of Al, which is performed by introducing Ga as a background donor dopant. The concentration of V_{Zn} is found to hold a quadratic dependence on the Al-doping concentration, evidencing the prevailing -2 charge state of V_{Zn} in n -ZnO. Further, the diffusion of Al is well described at different donor background concentrations using a reaction-diffusion model, which also accounts for the diffusion and redistribution of the Ga background donors. In predoped ZnO, the Al diffusion is strongly influenced by the high free-charge-carrier concentration (Ga donors) and gives rise to Al vs depth profiles that are very different from those in undoped ZnO. The effective diffusivity of Al is enhanced in the predoped sample, which is attributed to the higher abundance of the mediating V_{Zn}^{2-} . Using state-of-the-art DFT results from the literature [39] as input in the reaction-diffusion simulations, we obtain a migration barrier of the $(\text{Al}_{\text{Zn}}V_{\text{Zn}})^-$ pair of 2.4 ± 0.2 eV. This value is extracted independently from the two different experiments using undoped and predoped samples, respectively. The value is also in close agreement with results from previous DFT predictions [39] (2.55 eV).

ACKNOWLEDGMENTS

We thank V. Prozheeva and N. Segercrantz for assistance with the PAS measurements and H. N. Riise for the growth of sputter-deposited films. Financial support from the Research Council of Norway for funding of the Norwegian

PhD Network on Nanotechnology for Microsystems (Grant No. 221860/F40), DYNAZOx-project (Grant No. 221992), Salient (Grant No. 239895), the University of Oslo, and the Norwegian Micro- and Nano-Fabrication Facility (NorFab Grant No. 197411/V30) is gratefully acknowledged.

-
- [1] T. M. Børseth, J. S. Christensen, K. Maknys, A. Hallén, B. G. Svensson, and A. Y. Kuznetsov, *Superlattices Microstruct.* **38**, 464 (2005).
- [2] N. H. Nickel, *Phys. Rev. B* **73**, 195204 (2006).
- [3] K. M. Johansen, J. S. Christensen, E. V. Monakhov, A. Y. Kuznetsov, and B. G. Svensson, *Appl. Phys. Lett.* **93**, 152109 (2008).
- [4] K. M. Johansen, L. Vines, T. S. Bjørheim, R. Schifano, and B. G. Svensson, *Phys. Rev. Appl.* **3**, 024003 (2015).
- [5] A. Y. Azarov, K. E. Knutsen, P. T. Neuvonen, L. Vines, B. G. Svensson, and A. Y. Kuznetsov, *Phys. Rev. Lett.* **110**, 175503 (2013).
- [6] A. Y. Azarov, A. Hallén, X. L. Du, P. Rauwel, A. Y. Kuznetsov, and B. G. Svensson, *Br. J. Appl. Phys.* **115**, 073512 (2014).
- [7] A. Azarov, L. Vines, P. Rauwel, E. Monakhov, and B. G. Svensson, *Br. J. Appl. Phys.* **119**, 185705 (2016).
- [8] P. T. Neuvonen, L. Vines, V. Venkatachalapathy, A. Zubiaga, F. Tuomisto, A. Hallén, B. G. Svensson, and A. Y. Kuznetsov, *Phys. Rev. B* **84**, 205202 (2011).
- [9] J.-i. Nomoto, M. Konagai, K. Okada, T. Ito, T. Miyata, and T. Minami, *Thin Solid Films* **518**, 2937 (2010).
- [10] D. C. Look, K. D. Leedy, L. Vines, B. G. Svensson, A. Zubiaga, F. Tuomisto, D. R. Douth, and L. J. Brillson, *Phys. Rev. B* **84**, 115202 (2011).
- [11] J. E. Stehr, K. M. Johansen, T. S. Bjørheim, L. Vines, B. G. Svensson, W. M. Chen, and I. A. Buyanova, *Phys. Rev. Appl.* **2**, 021001 (2014).
- [12] D. C. Look, J. W. Hemsky, and J. R. Sizelove, *Phys. Rev. Lett.* **82**, 2552 (1999).
- [13] A. F. Kohan, G. Ceder, D. Morgan, and C. G. Van de Walle, *Phys. Rev. B* **61**, 15019 (2000).
- [14] A. Janotti and C. G. Van de Walle, *Phys. Rev. B* **76**, 165202 (2007).
- [15] D. G. Thomas, *J. Phys. Chem. Solids* **3**, 229 (1957).
- [16] C. Bhodoo, A. Hupfer, L. Vines, E. V. Monakhov, and B. G. Svensson, *Phys. Rev. B* **94**, 205204 (2016).
- [17] L. Vines and A. Kuznetsov, in *Oxide Semiconductors, Semiconductors and Semimetals* Vol. 88 (Elsevier/Academic, San Diego, 2013), p. 67.
- [18] L. Vines, E. V. Monakhov, R. Schifano, W. Mtangi, F. D. Auret, and B. G. Svensson, *Br. J. Appl. Phys.* **107**, 103707 (2010).
- [19] K. M. Johansen, A. Zubiaga, I. Makkonen, F. Tuomisto, P. T. Neuvonen, K. E. Knutsen, E. V. Monakhov, A. Y. Kuznetsov, and B. G. Svensson, *Phys. Rev. B* **83**, 245208 (2011).
- [20] A. Janotti and C. G. Van de Walle, *J. Cryst. Growth* **287**, 58 (2006).
- [21] D. O. Demchenko, B. Earles, H. Y. Liu, V. Avrutin, N. Izyumskaya, Ü. Özgür, and H. Morkoç, *Phys. Rev. B* **84**, 075201 (2011).
- [22] Y. K. Frodason, K. M. Johansen, T. S. Bjørheim, B. G. Svensson, and A. Alkauskas, *Phys. Rev. B* **95**, 094105 (2017).
- [23] F. Tuomisto, V. Ranki, K. Saarinen, and D. C. Look, *Phys. Rev. Lett.* **91**, 205502 (2003).
- [24] F. Tuomisto, K. Saarinen, D. C. Look, and G. C. Farlow, *Phys. Rev. B* **72**, 085206 (2005).
- [25] T. N. Sky, K. M. Johansen, H. N. Riise, B. G. Svensson, and L. Vines, *Br. J. Appl. Phys.* **123**, 055701 (2018).
- [26] W. Lin, K. Ding, Z. Lin, J. Zhang, J. Huang, and F. Huang, *Cryst. Eng. Commun.* **13**, 3338 (2011).
- [27] F. Tuomisto and I. Makkonen, *Rev. Mod. Phys.* **85**, 1583 (2013).
- [28] S. Valkealahti and R. M. Nieminen, *Appl. Phys. A* **32**, 95 (1983).
- [29] S. Valkealahti and R. M. Nieminen, *Appl. Phys. A* **35**, 51 (1984).
- [30] H. E. Hansen and U. Ingerslev-Jensen, *J. Phys. D* **16**, 1353 (1983).
- [31] V. Prozheeva, K. M. Johansen, P. T. Neuvonen, A. Zubiaga, L. Vines, A. Y. Kuznetsov, and F. Tuomisto, *Mater. Sci. Semicond. Process.* **69**, 19 (2017).
- [32] A. Zubiaga, F. Tuomisto, V. A. Coleman, H. H. Tan, C. Jagadish, K. Koike, S. Sasa, M. Inoue, and M. Yano, *Phys. Rev. B* **78**, 035125 (2008).
- [33] F. Tuomisto, in *Semiconductors and Semimetals*, Oxide Semiconductors, Vol. 88 (Academic, San Diego, 2013), Chap. 2, pp. 39–65.
- [34] H. Y. Liu, V. Avrutin, N. Izyumskaya, M. A. Reshchikov, Ü. Özgür, and H. Morkoç, *Phys. Status Solidi RRL* **4**, 70 (2010).
- [35] T. Minami, *Semicond. Sci. Technol.* **20**, S35 (2005).
- [36] D. C. Look, K. D. Leedy, D. H. Tomich, and B. Bayraktaroglu, *Appl. Phys. Lett.* **96**, 062102 (2010).
- [37] T. Nakagawa, I. Sakaguchi, M. Uematsu, Y. Sato, N. Ohashi, H. Haneda, and Y. Ikuhara, *Jpn. J. Appl. Phys.* **46**, 4099 (2007).
- [38] E. Antoncik, *J. Electrochem. Soc.* **142**, 3170 (1995).
- [39] D. Steiauf, J. L. Lyons, A. Janotti, and C. G. V. de Walle, *APL Mater.* **2**, 096101 (2014).
- [40] J. T-Thienprasert, S. Rujirawat, W. Klysubun, J. N. Duenow, T. J. Coutts, S. B. Zhang, D. C. Look, and S. Limpijumng, *Phys. Rev. Lett.* **110**, 055502 (2013).
- [41] P. M. Fahey, P. B. Griffin, and J. D. Plummer, *Rev. Mod. Phys.* **61**, 289 (1989).
- [42] E. Antoncik, *Phys. Status Solidi A* **149**, 557 (1995).
- [43] R. Hauschild, H. Priller, M. Decker, J. Brückner, H. Kalt, and C. Klingshirn, *Phys. Status Solidi C* **3**, 976 (2006).
- [44] M. Uematsu, *Br. J. Appl. Phys.* **82**, 2228 (1997).
- [45] H. Bracht, *Phys. Rev. B* **75**, 035210 (2007).
- [46] A. Azarov, V. Venkatachalapathy, Z. Mei, L. Liu, X. Du, A. Galeckas, E. Monakhov, B. G. Svensson, and A. Kuznetsov, *Phys. Rev. B* **94**, 195208 (2016).